

Two-Dimensional ENDOR-ESEEM Correlation Spectroscopy

G. Bar,* A. Pöpl,† S. Vega,* and D. Goldfarb*

*Department of Chemical Physics, Weizmann Institute of Science, Rehovot 76100, Israel; and †Faculty of Physics and Geoscience, University of Leipzig, Linnéstrasse 5, D-04103 Leipzig, Germany

Received December 29, 1999; revised March 17, 2000

A two-dimensional (2D) experiment that correlates electron-nuclear double resonance (ENDOR) and electron spin-echo envelope modulation (ESEEM) frequencies, useful for unraveling and assigning ENDOR and ESEEM spectra from different paramagnetic centers with overlapping EPR spectra, is presented. The pulse sequence employed is similar to the Davies ENDOR experiment with the exception that the two-pulse echo detection is replaced by a stimulated echo detection in order to enhance the resolution in the ESEEM dimension. The two-dimensional data set is acquired by measuring the ENDOR spectrum as a function of the time interval T between the last two microwave pulses of the stimulated echo detection scheme. This produces a series of ENDOR spectra with amplitudes that are modulated with T . Fourier transformation (FT) with respect to T then generates a 2D spectrum with cross peaks connecting spectral lines of the ESEEM and ENDOR spectra that belong to the same paramagnetic center. Projections along the vertical and horizontal axes give the three-pulse FT-ESEEM and ENDOR spectra, respectively. The feasibility of the experiment was tested by simulating 2D ENDOR-ESEEM correlation spectra of a system consisting of an electron spin ($S = \frac{1}{2}$) coupled to two nuclei ($I_1 = I_2 = \frac{1}{2}$), taking into account experimental conditions such as pulse durations and off-resonance irradiation frequencies. The experiment is demonstrated on a single crystal of Cu^{2+} doped L-histidine (Cu-His), containing two symmetrically related Cu^{2+} sites that at an arbitrary orientation exhibit overlapping ESEEM and ENDOR spectra. While the ESEEM spectrum is relatively simple and arises primarily from one weakly coupled ^{14}N , the ENDOR spectrum is very crowded due to contributions from two nonequivalent nitrogens, two chlorides, and a relatively large number of protons. The simple ESEEM projection of the 2D ENDOR-ESEEM correlation spectrum is then used to disentangle the ENDOR spectrum and resolve two sets of lines corresponding to the different sites. © 2000 Academic Press

Key Words: pulsed EPR; two-dimensional spectroscopy; ENDOR.

INTRODUCTION

Ligand hyperfine and nuclear quadrupole interactions are major sources of information for understanding both the electronic and the geometric structure of paramagnetic centers. These interactions are, however, usually small and not resolved in EPR spectra. They are best determined by electron-nuclear

double resonance (ENDOR) (1–3) or by electron spin-echo envelope modulation (ESEEM) spectroscopies (4–8). At X-band frequencies these two methods are complementary; the ENDOR techniques are most suitable for relatively large couplings, whereas the ESEEM methods are most effective when small hyperfine interactions, in the order of the nuclear Zeeman interactions, are involved. The assignment of the peaks in ENDOR or ESEEM spectra is often a difficult task due to overlapping signals arising from different nuclei and several paramagnetic centers. The development of two-dimensional (2D) correlation spectroscopy has offered new possibilities for the interpretation of complex ESEEM and ENDOR spectra (9–17). The detection of spectral correlations and the enhanced resolution due to the spread of the spectra into a second dimension facilitates considerably signal assignments. An example is the 2D hyperfine sublevel correlation (HYSCORE) experiment, which has revolutionized the field of ESEEM spectroscopy (10, 18). In this experiment correlations between nuclear frequencies belonging to the same paramagnetic center and different M_s manifolds are obtained. Another example is the complementary 2D DONUT-HYSCORE experiment (12) which provides frequency correlations within a particular M_s manifold. In this publication we present a new 2D experiment that correlates ENDOR and ESEEM frequencies and is useful for unraveling and assigning ENDOR and ESEEM signals from different paramagnetic centers with overlapping EPR spectra.

The 2D ENDOR-ESEEM correlation experiment, shown in Fig. 1a, is an extension of the existing 1D experiments, termed ENDOR-edited ESEEM and ESEEM-edited ENDOR, introduced by Thomann and Bernardo (19). These experiments were designed to differentiate between ENDOR lines of two centers, one exhibiting nuclear modulation and the other not. In the first version of these experiments a difference spectrum of two Davies-ENDOR spectra obtained with two different τ values, chosen according to the first minimum and maximum of the two-pulse ESEEM time domain pattern, is recorded. ENDOR lines that are independent of τ vanish, leaving only lines belonging to the center that experiences nuclear modulation. In the second version, two-pulse ESEEM signals are detected as a function of τ during on- and off-resonance RF

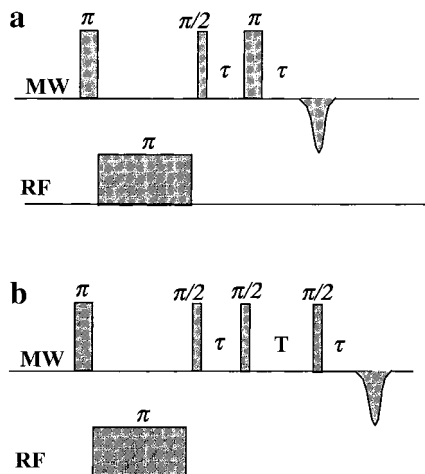


FIG. 1. The pulse sequences of (a) two- and (b) three-pulse 2D ENDOR-ESEEM correlation experiments.

irradiation on an ENDOR transition. The difference spectrum, obtained by subtraction of these ESEEM signals followed by Fourier transformation (FT), reveals ESEEM frequencies originating from EPR transitions that have a common level with the selected ENDOR transition. These combined experiments were applied to distinguish between two FeS centers in oxidized hydrogenase, where both centers exhibit an ENDOR spectrum but only one experiences nuclear modulations (19).

In the 2D version of the experiment the frequency of both the RF pulse and τ are varied and FT of the τ dependent echo

amplitude is performed to obtain a 2D spectrum. Prior to the FT, the effect of the RF is isolated by subtracting from each ENDOR slice the intensity of the first (off-resonance) frequency point, which is equivalent to taking the difference between ESEEM spectra recorded with and without RF pulses (see above). The resulting 2D spectrum exhibits cross peaks between ESEEM and ENDOR frequencies that belong to the same paramagnetic center, whereas projections along the two axes give the FT-ESEEM and ENDOR spectra.

The effect of the 2D pulse sequence is demonstrated on a simple spin system of an electron spin with $S = \frac{1}{2}$ coupled to two nuclei, $I_1 = \frac{1}{2}$ and $I_2 = \frac{1}{2}$, with a large hyperfine coupling to the first nucleus (a_1) and a small coupling to the second nucleus (a_2). Thus, the first interaction results in an easily detectable ENDOR spectrum and the second in a nuclear modulation effect (ESEEM spectrum). The changes of the energy level populations during the experiment are followed and illustrated in Fig. 2, where both couplings are assumed to be positive and smaller than the nuclear Larmor frequency ω_I . The energies in the diagram of Fig. 2 are assigned according to the spin-down $|\beta\rangle$ and spin-up $|\alpha\rangle$ states of the electron and the first and the second nucleus, respectively (from left to right). The first microwave (MW) π pulse in Fig. 1a is selective with respect to the large coupling and leads to a population inversion of two of the four allowed EPR transitions, $\{|\beta\alpha\alpha\rangle - |\alpha\alpha\alpha\rangle\}$ and $\{|\beta\alpha\beta\rangle - |\alpha\alpha\beta\rangle\}$, while leaving the other two, $\{|\beta\beta\alpha\rangle - |\alpha\beta\alpha\rangle\}$ and $\{|\beta\beta\beta\rangle - |\alpha\beta\beta\rangle\}$, unchanged. The application of a two-pulse echo detection sequence at the same

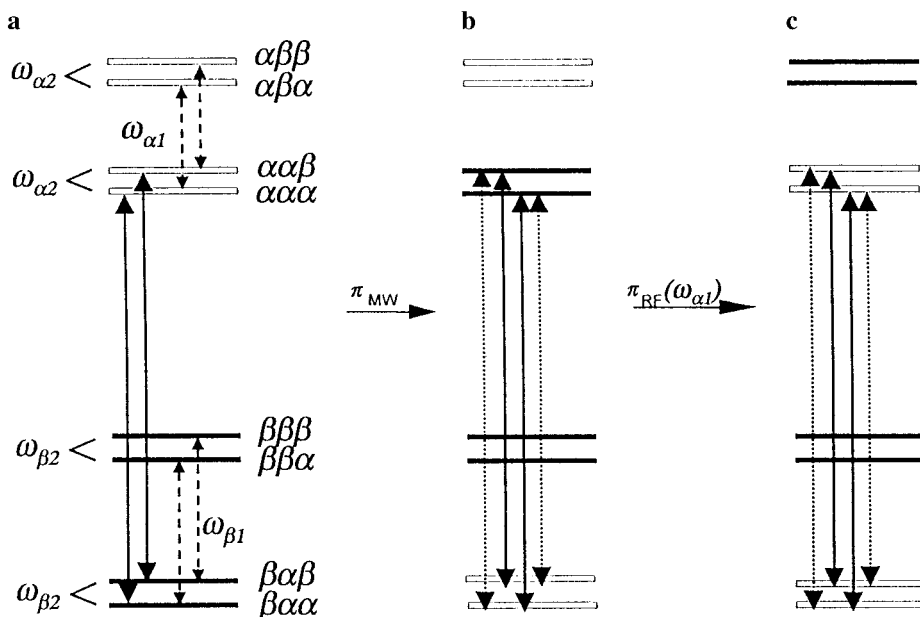


FIG. 2. Energy-level diagram and the evolution of the energy level populations of a $S = \frac{1}{2}$, $I_1 = \frac{1}{2}$, $I_2 = \frac{1}{2}$ system (with hyperfine couplings a_1 and a_2 and $\omega_{\beta 1} = \omega_{\beta 2} > a_1 > a_2 > 0$) during the ENDOR-ESEEM correlation experiment for a. Black bars correspond to higher populations whereas empty bars to lower populations. Allowed EPR transitions are indicated by solid arrows while the forbidden transitions are marked by dotted arrows. The NMR transitions of I_1 are marked with dashed arrows.

MW frequency results then in a negative echo amplitude. Repeating the experiment, while incrementing the τ interval between the two pulses, generates a decaying echo amplitude that is modulated with frequencies $\omega_{\alpha 2}$ and $\omega_{\beta 2}$, corresponding to the $\{|\alpha\alpha\alpha\rangle - |\alpha\alpha\beta\rangle\}$ and $\{|\beta\alpha\alpha\rangle - |\beta\alpha\beta\rangle\}$ nuclear transitions of I_2 . The nuclear modulation is a consequence of the mixing of the allowed and forbidden ESR transitions indicated in Fig. 2B (6). If, prior to the two-pulse echo sequence, an RF π pulse is applied at the $\omega_{\alpha 1}$ frequency of I_1 , the additional population inversions of the $\{|\alpha\alpha\alpha\rangle - |\alpha\alpha\beta\rangle\}$ and $\{|\alpha\alpha\beta\rangle - |\alpha\beta\beta\rangle\}$ transitions (Fig. 2C) alter the two-pulse echo amplitude and a difference between the ESEEM signal obtained with and without this RF pulse is expected. The ESEEM and ENDOR frequencies that are connected by a common EPR transition will contribute to the difference ESEEM spectrum. The ability of the MW π pulse to selectively invert EPR transitions enables the correlation between ESEEM lines arising from the weak hyperfine interaction and the ENDOR lines originating from the strong interaction. If the inversion MW pulse would be selective also with respect to the small coupling, for example inverting only the $\{|\beta\alpha\alpha\rangle - |\alpha\alpha\alpha\rangle\}$ EPR transition, then an experiment similar to TRIPLE (21, 22), correlating ESEEM and ENDOR lines corresponding to the same M_S manifold only, is obtained.

In practice, the 2D experiment described above suffers from a low resolution in the ESEEM dimension, caused by the relatively fast decay of the two-pulse echo in solids. This can be circumvented by replacing the two-pulse echo detection sequence ($\pi/2-\tau-\pi-\tau$) by a stimulated echo sequence ($\pi/2-\tau-\pi/2-T-\pi/2-\tau$), as shown in Fig. 1b. In this experiment τ is held constant and T is incremented. Since the ESEEM generated by the stimulated echo suffers from blind spots (5), it is advisable to repeat the experiment for several τ values in order to ensure detection of all ESEEM frequencies. In addition, a four-step phase cycling of the detection sequence is necessary in order to eliminate interferences from unwanted echoes (23).

The feasibility of this 2D experiment was first tested theoretically and then demonstrated experimentally on a single crystal of Cu(II) doped L-histidine HCl \cdot H₂O. The space group of the crystal is P2₁2₁2₁ and two crystallographic sites are present that both contribute to the EPR, ESEEM, and ENDOR spectra (24). This crystal has been a subject of many investigations and the hyperfine and quadrupole tensors of the coupled nuclei are known (18, 24–26). In this crystal the copper ion is coordinated to the amino nitrogen of one histidine molecule and to the imidazole nitrogen of another histidine molecule. In addition, it is bound to a third histidine molecule through its carboxylic oxygen, a water molecule, and two chloride ions. This coordination structure makes the ENDOR spectrum of each Cu(II) congested and complicated as it consists of lines arising from two strongly coupled ¹⁴N nuclei (amino and imino), a number of protons, and two ^{35,37}Cl nuclei. In contrast, the ESEEM spectrum is considerably simpler as it is dominated by low-frequency signals due to a single weakly

coupled remote ¹⁴N nitrogen in the imidazole. Consequently, through the correlations between the simple ESEEM spectrum and the ENDOR spectra, the subspectra corresponding to the two sites can be distinguished.

EXPERIMENTAL

Sample Preparation

CuCl₂ (0.5% mol) was added to an aqueous solution of 98% L-histidine HCl \cdot H₂O (18). Slow evaporation at room temperature over a period of a few days generated large crystals.

Spectroscopic Measurement

Pulsed EPR and ENDOR measurements were performed at X-band at 12 K on a Bruker ESP 380 spectrometer. Echo-detected (ED) EPR measurements were done using the two-pulse echo sequence $\{\pi/2-\tau-\pi-\tau\}$ with pulse lengths of 24/48 ns. Typical MW pulse widths for the two-pulse and three-pulse ESEEM experiments were the same as in the ED EPR experiment. The ENDOR spectra were collected with either selective MW pulses, $t_{MW,\pi/2} = 100$ ns, $t_{MW,\pi} = 200$ ns, or with nonselective pulses, $t_{MW,\pi/2} = 24$ ns, $t_{MW,\pi} = 48$ ns. The RF pulse length, t_{RF} , in the Davies-ENDOR experiment was 8 μ s. In 1D ENDOR experiments 1024 points were sampled with a RF step width, ΔRF , of 0.02 MHz. A 2D data set of 512×1024 points (RF \times time) was recorded in the 2D experiments with $\Delta RF = 0.04$ MHz and a dwell time $\Delta T = 16$ ns. A typical repetition rate was 2 ms. A four-step phase cycle was employed in all experiments involving the three-pulse ESEEM sequence to remove interfering echoes (23).

Data Manipulation

The time domain 1D ESEEM data were treated using Bruker WINEPR software. The manipulation included baseline correction, zero filling, Fourier transform, and magnitude mode calculation. In the case of the ENDOR-ESEEM correlation experiment, baseline corrections were carried out for both frequency and time domains. In each ENDOR (RF) slice the value of the intensity of the first frequency point was subtracted from all other points, yielding the appropriate difference spectrum. Then FT was carried out in the time domain, followed by a magnitude calculation.

Simulations

A computer program has been designed to calculate 1D and 2D spectra that are obtained from pulse EPR, ENDOR, and ESEEM experiments on a system of one electron spin $S = \frac{1}{2}$ coupled to two or more nonequivalent nuclei with spins $I = \frac{1}{2}$ or 1. For simplicity, we describe the methodology of computation considering an electron coupled to two nuclei with $I_1 = I_2 = \frac{1}{2}$. This system has a spin Hamiltonian of the form

$$\mathcal{H}_0 = \omega_S S_z + \sum_{j=1}^2 (S \cdot \mathbf{A}_j \cdot I_j - \omega_{Ij} I_{zj}), \quad [1]$$

where $\omega_S = \beta g B_0 / \hbar$ and $\omega_{Ij} = \beta_n g_{nj} B_0 / \hbar$. The three terms in Eq. [1] are the electron Zeeman interaction, assuming an isotropic g value, the hyperfine interaction, and the nuclear Zeeman term. β is the electron Bohr magneton constant, β_n is the nuclear magneton constant, and g_{nj} is the isotropic nuclear g -factor. The principal values of the hyperfine tensors, \mathbf{A}_j , are A_{xxj} , A_{yyj} , and A_{zzj} . In the case that one of the nuclei has a spin $I > \frac{1}{2}$ a nuclear quadrupole interaction term should be added.

During a MW or RF pulse the following irradiation terms must be added to the Hamiltonian:

$$\mathcal{H}_{\text{MW}}(t) = 2\omega_{1S} S_x \cos(\omega_{\text{MW}} t + \phi_{\text{MW}}) \quad [2]$$

$$\mathcal{H}_{\text{RF}}(t) = 2\omega_{1I} \sum_j I_{xj} \cos(\omega_{\text{RF}} t + \phi_{\text{RF}}), \quad [3]$$

where ω_{1S} , ω_{1I} , and ϕ_{MW} , ϕ_{RF} are the intensities and phases of the MW and RF fields, and ω_{MW} and ω_{RF} are their corresponding frequencies, respectively. The effects of the RF irradiation on the EPR transitions and that of the MW irradiation on the ENDOR transitions are ignored, thus the hyperfine enhancement factor is not taken into account (2). The EPR signals are detected in the rotating frame of the MW frequency field and the MW rotating frame Hamiltonian, $\mathcal{H}_0^{\text{R}}(t)$, is

$$\begin{aligned} \mathcal{H}_0^{\text{R}}(t) = & \Delta\omega_S S_z \\ & + \sum_{j=1}^2 (A_{zxxj} S_z I_{xj} + A_{zyj} S_z I_{yj} + A_{zzj} S_z I_{zj} - \omega_{0I} I_{zj}) \\ & + \omega_{1S}(t) (S_x \cos \phi_{\text{MW}} + S_y \sin \phi_{\text{MW}}) \\ & + 2\omega_{1I}(t) \sum_{j=1}^2 I_{xj} \cos(\omega_{\text{RF}} t + \phi_{\text{RF}}), \end{aligned} \quad [4]$$

where $\Delta\omega_S = \omega_S - \omega_{\text{MW}}$. The time-dependent MW and RF fields, introduced in Eq. [4], are zero between the pulses and equal to ω_{1S} and ω_{1I} during the pulses, respectively. The RF term commutes with the rotating frame transformation operator $e^{-i\omega_{\text{MW}}(t_f - t_i) S_z}$ and therefore stays time dependent in this frame. In $\mathcal{H}_0^{\text{R}}(t)$ the time-dependent hyperfine terms that include the operators S_x and S_y were neglected because they are assumed to be small, $\omega_S \gg |A|$.

The time response of the spin system to this Hamiltonian is evaluated by solving the Liouville–von Neumann equation for the spin density operator $\rho(t)$ in the rotating frame,

$$\rho(t_f) = U(t_i, t_f) \rho(t_i) U^{-1}(t_i, t_f), \quad [5]$$

where $U(t_i, t_f)$ is the evolution propagator defined by the Hamiltonian $\mathcal{H}_0^{\text{R}}(t)$ in the time interval between t_i and t_f . Using the high field approximation the initial density matrix $\rho(0)$ at the start of each experiment is

$$\rho(0) \propto S_z + \sum_{j=1}^2 (g_{nj} \beta_n / g \beta) I_{zj}. \quad [6]$$

Three types of time domains can be distinguished in the experiments and accordingly three evolution propagators, $U(t_i, t_f)$, are used. During free precession and MW irradiation the Hamiltonian is time independent and

$$U_{0,\text{MW}}(t_i, t_f) = \exp\{-i\mathcal{H}_0^{\text{R}}(t_f - t_i)\}, \quad [7]$$

where \mathcal{H}_0^{R} is the spin Hamiltonian with $\omega_{1I}(t) = 0$ and the value of $\omega_{1S}(t)$ equals zero and ω_{1S} , respectively. During the third time domain the RF pulse is on and $\mathcal{H}_0^{\text{R}}(t)$ is time dependent. To evaluate the evolution propagator during an RF pulse starting at a time t_i the Hamiltonian is transformed to the doubly rotating frame, defined by an additional transformation (27):

$$U'(t_i, t_f) = \exp\{-i\omega_{\text{RF}} I_{z1} + I_{z2}(t_f - t_i)\}. \quad [8]$$

In this frame the Hamiltonian with $\omega_S(t) = 0$ becomes equal to

$$\begin{aligned} \mathcal{H}_0^{\text{DR}}(t) = & \Delta\omega_S S_z + \sum_{j=1}^2 [A_{zzj} S_z I_{zj} - \Delta\omega_{Ij} I_{zj}] \\ & + \sum_{j=1}^2 \omega_{1S} (I_{xj} \cos \phi_{\text{RF}} + I_{yj} \sin \phi_{\text{RF}}) \\ & + \sum_{j=1}^2 e^{i\omega_{\text{RF}}(t_f - t_i) I_{zj}} (A_{zxx} S_z I_{xj} \\ & + A_{zy} S_z I_{yj}) e^{-i\omega_{\text{RF}}(t_f - t_i) I_{zj}}. \end{aligned} \quad [9]$$

and stays time dependent. In Eq. [9] $\Delta\omega_{Ij} = \omega_{Ij} - \omega_{\text{RF}}$. The evolution operator during the RF pulse in the MW rotating frame can then be evaluated by (27)

$$U_{\text{RF}}(t_i, t_f) = U'(t_i, t_f) T \exp\left\{-i \int_{t_i}^{t_f} \mathcal{H}_0^{\text{DR}}(t) dt\right\}, \quad [10]$$

where T is the Dyson ordering operator. For the actual calculations of $U_{\text{RF}}(t_i, t_f)$ in Eq. [10] the Dyson operator was replaced by a numerical stepwise integration. When the RF

field intensity is much stronger than the anisotropic parts of the hyperfine coupling, the time-dependent terms of $\mathcal{H}_0^{\text{DR}}(t)$ can be ignored and the evolution operator can be calculated straightforwardly by a simple integration of the time-independent Hamiltonian.

The calculations were performed in a matrix representation of the spin Hamiltonian and the density operator and when necessary the Hamiltonian was diagonalized to enable the calculation of $U(t_i, t_f)$ according to

$$\begin{aligned} U(t_i, t_f) &= \exp\{-i\mathcal{H}(t_f - t_i)\} \\ &= V(\exp(-i\Lambda(t_f - t_i)))V^{-1}, \end{aligned} \quad [11]$$

where Λ is the diagonal form of \mathcal{H} obtained by $\Lambda = V^{-1}\mathcal{H}V$. Successive application of the evolution propagators of the MW, RF, and free evolution time domains on the initial spin density matrix enables the calculation of the EPR signal defined by

$$M_-(t) = \text{tr}(\rho(t)S_-). \quad [12]$$

For the simulations of 2D ENDOR-ESEEM correlation spectra a full calculation was performed for each RF irradiation and each T value. The resulting echo intensities, given by $M_-(\omega_{\text{RF}}, T)$, were Fourier transformed and a 2D spectrum $M_-(\omega_{\text{ENDOR}}, \omega_{\text{ESEEM}})$ was obtained with $\omega_{\text{ENDOR}} = \omega_{\text{RF}}$ and ω_{ESEEM} being the frequency parameter of the FT of the stimulated echo intensities.

In actual experiments unwanted signal components, which are created due to the finite intensities and durations of the MW and RF pulses, are eliminated by phase cycling (28). In the calculations signals corresponding to unwanted echoes and FIDs, originating from the stimulated echo sequence, were also eliminated by phase cycling. Unwanted FID signals do not interfere in the experiments since the inhomogeneous line broadening causes them to decay within the spectrometer dead time. To eliminate unwanted nuclear coherences, all off-diagonal elements of the density matrix corresponding to these coherences were set to zero before and after the RF pulse application. This approach is valid when the applied RF pulse is designed to induce changes in the populations of the energy levels which are represented exclusively by diagonal elements. This procedure shortens the computation time, but must be performed with some care. For example, during the ESEEM pulse sequence the nuclear spin coherences are responsible for the stimulated echo modulation and must, therefore, be retained. Actual relaxation phenomena during the experiments were taken into account by introducing a nuclear, T_{2n} , and an electronic spin-spin, T_{2e} , relaxation parameter and multiplying the appropriate matrix elements during the free precession periods by $e^{-t/T_{2n}}$ and $e^{-t/T_{2e}}$, respectively.

RESULTS

Simulations

The simulations of the ENDOR-ESEEM correlation experiment were carried out on a relatively simple system of two ^{15}N nuclei ($I = \frac{1}{2}$) coupled to a single electron ($S = \frac{1}{2}$). One nitrogen, $^{15}\text{N}_{(1)}$, has a large isotropic hyperfine interaction, $A_{\text{iso}1} = 42.35$ MHz, and the second, $^{15}\text{N}_{(2)}$, has a smaller and anisotropic hyperfine interaction ($A_{xx2} = 1.787$, $A_{yy2} = 1.488$, $A_{zz2} = 2.442$ MHz). These hyperfine values where

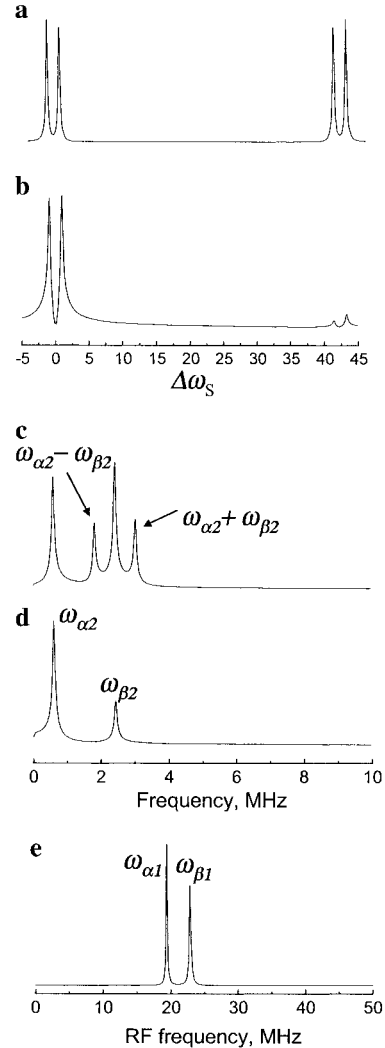


FIG. 3. (a) A simulated FT-EPR spectrum of a $S = \frac{1}{2}$, $I_1 = I_2 = \frac{1}{2}$ system. $A_{\text{iso}1} = 42.35$ MHz, $A_{xx2} = 1.787$ MHz, $A_{yy2} = 1.488$ MHz, $A_{zz2} = 2.442$ MHz, $t_{\text{MW},\pi/2} = 0.25$ ns, $B_0 = 3500$ G, and $\omega_{\text{MW}} = 9.829$ GHz; (b) same with selective pulses, $t_{\text{MW},\pi/2} = 100$ ns; (c) two-pulse; and (d) three-pulse FT-ESEEM spectra of the same system and conditions as in (b), $t_{\text{MW},\pi/2} = 100$ ns. (e) A simulated Davies ENDOR spectrum for the same system, $t_{\text{MW},\pi/2} = 100$ ns, $t_{\text{MW},\pi} = 200$ ns, $t_{\text{RF}} = 5$ μs , $\Delta\text{RF} = 0.2$ MHz; The Euler angles giving the orientation of the hyperfine tensor of $^{15}\text{N}_2$ with respect to the crystal axes are 67° , 112° , 11° , and those describing the crystal orientation with respect to the magnetic field are 90° , 37° , 0° .

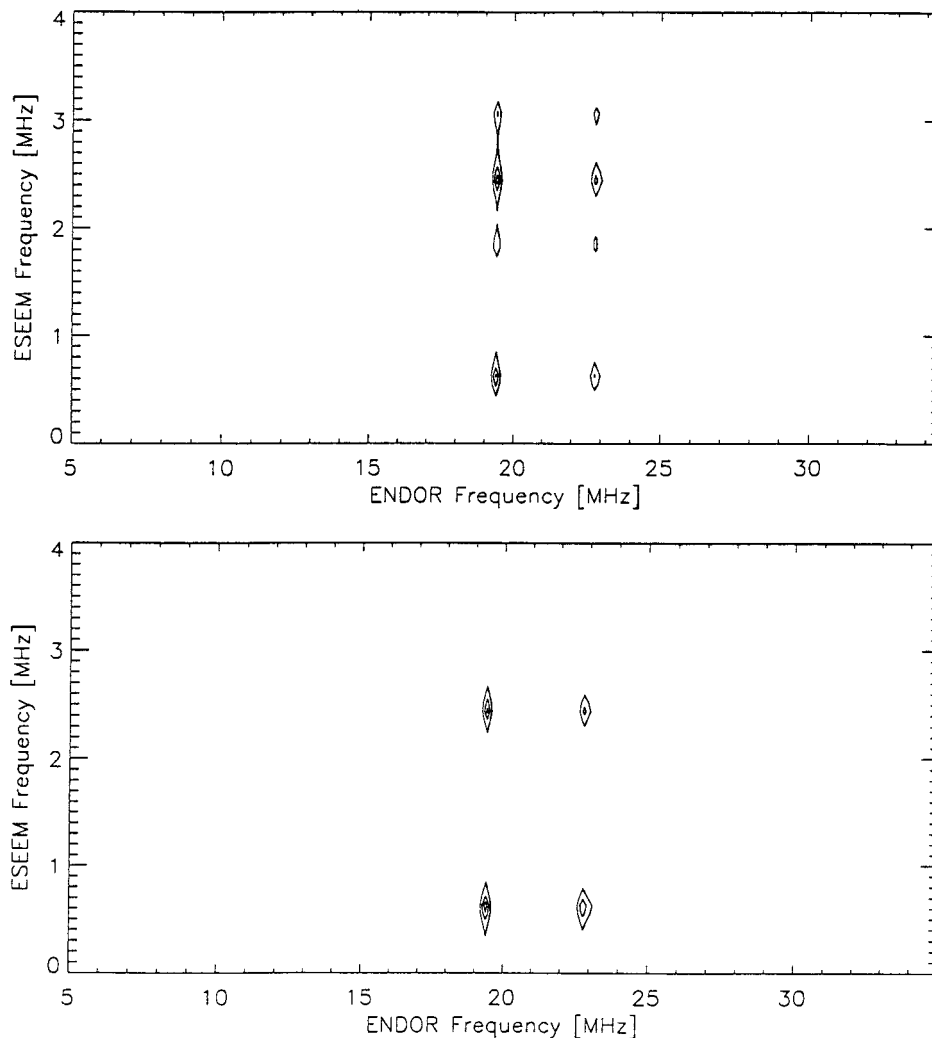


FIG. 4. Simulated 2D ENDOR-ESEEM correlation spectra obtained with (top) two-pulse and (bottom) three-pulse detection sequences. The simulation parameters are as in Figs. 3c–3e.

taken from the ^{14}N coupling parameters of the Cu-His crystal (25). For typical experimental conditions of an X-band spectrometer the ENDOR spectrum shows only signals from $^{15}\text{N}_{(1)}$, because the frequencies of $^{15}\text{N}_{(2)}$ are too low to be detected. In contrast, only interactions with $^{15}\text{N}_{(2)}$ will contribute to the ESEEM spectrum. The reason for the absence of the $^{15}\text{N}_{(1)}$ signals in this case is the vanishing anisotropic hyperfine interaction necessary for the observation of nuclear modulation. However, even if a significant anisotropic hyperfine interaction would have been present, the bandwidth of a typical MW pulse is not sufficient to excite concomitantly allowed and forbidden ESR transitions, which is essential for the observation of ESEEM.

The MW and RF pulse lengths, amplitudes, and frequencies used for the ENDOR-ESEEM correlation simulations were determined as follows. First, the FID EPR signal at a particular magnetic field was simulated using a single, very short $\pi/2$ pulse that covers all four EPR transitions. Fourier transforma-

tion of the FID produced an EPR spectrum, shown in Fig. 3a, which consists of two doublets, separated by 42.35 MHz, with an inner doublet splitting of 1.85 MHz. The frequencies of the four hyperfine components were then determined and the MW carrier frequency (ω_{MW}) was set to the center of the lowest frequency EPR doublet. The MW pulse intensity, ω_{15} , and length, t_{MW} , were adjusted to excite only this particular doublet. The simulated FT-EPR spectrum obtained from this selective excitation is shown in Fig. 3b. These parameters were then used to simulate the two-pulse and three-pulse ESEEM and Davies ENDOR spectra presented in Figs. 3c, 3d, and 3e, respectively. The ENDOR spectrum shows only signals of $^{15}\text{N}_{(1)}$, namely a doublet centered at 21.17 MHz ($=A_{\text{iso1}}/2$), with a splitting of 3.0 MHz corresponding to twice the ^{15}N Larmor frequency, $\nu_{^{15}\text{N}}$. The signals of $^{15}\text{N}_{(2)}$ are absent, since the MW pulse width is nonselective with respect to its hyperfine coupling. The two-pulse ESEEM spectrum, obtained after FT of the modulated echo decay, shows four peaks, all originating

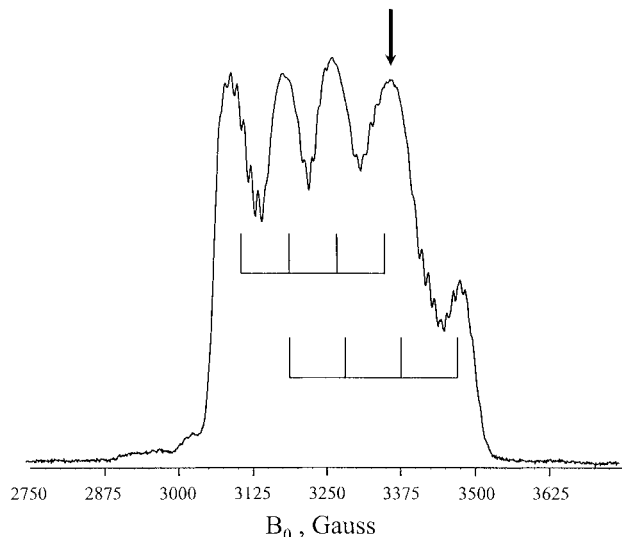


FIG. 5. ED-EPR spectrum of a Cu-His single crystal at an arbitrary orientation. $\nu_{\text{MW}} = 9.7348$ GHz, $t_{\text{MW},\pi/2} = 24$, $t_{\text{MW},\pi} = 48$ ns, $\tau = 200$ ns, $T = 12$ K. The two sets of $^{63,65}\text{Cu}$ hyperfine components are indicated in the figure. The arrow marks the magnetic field at which the pulse experiments were performed.

from $^{15}\text{N}_{(2)}$, with two peaks corresponding to the $(\omega_{\alpha 2}, \omega_{\beta 2})$ doublet centered at $\nu_{^{15}\text{N}}$ and two combination peaks at $\omega_{\alpha 2} \pm \omega_{\beta 2}$. The three-pulse ESEEM spectrum shows only the fundamental frequencies $\omega_{\alpha 2}$ and $\omega_{\beta 2}$. Simulations of the two-pulse

and three-pulse 2D ENDOR-ESEEM correlation spectra, calculated with the same set of parameters employed for the 1D spectra simulations, are shown in Fig. 4. Projections along the vertical axis yield the ESEEM spectra shown in Figs. 3c and 3d, whereas the projection along the horizontal axis corresponds to the ENDOR spectrum shown in Fig. 3e. In both spectra correlations appear between all ENDOR and ESEEM frequencies, as expected.

Experimental Results

The ED-EPR spectrum of a Cu-His single crystal, placed at an arbitrary orientation with respect to the magnetic field, is shown in Fig. 5. The spectrum consists of two overlapping quartets, corresponding to the two Cu^{2+} sites. The magnetic field chosen for the pulsed experiments was 3367 G, where the spectra of the two sites overlap. The ESEEM spectrum, shown in Fig. 6, exhibits two sets of peaks. The first consists of a few intense lines grouped in the low-frequency region, 0–4 MHz, that originate from the remote ^{14}N of the imidazole moiety (18). Only 6 of the total 12 expected lines (6 for each site) appear. The absence of some lines is not surprising since the ESEEM intensities depend on the crystal orientation and, in the three-pulse ESEEM, also on the time interval τ (5). The second group of lines appears in the 10- to 20-MHz region and it consists primarily of ^1H lines, while the appearance of some contributions from strongly coupled ^{14}N and $^{35,37}\text{Cl}$ nuclei cannot be excluded (25).

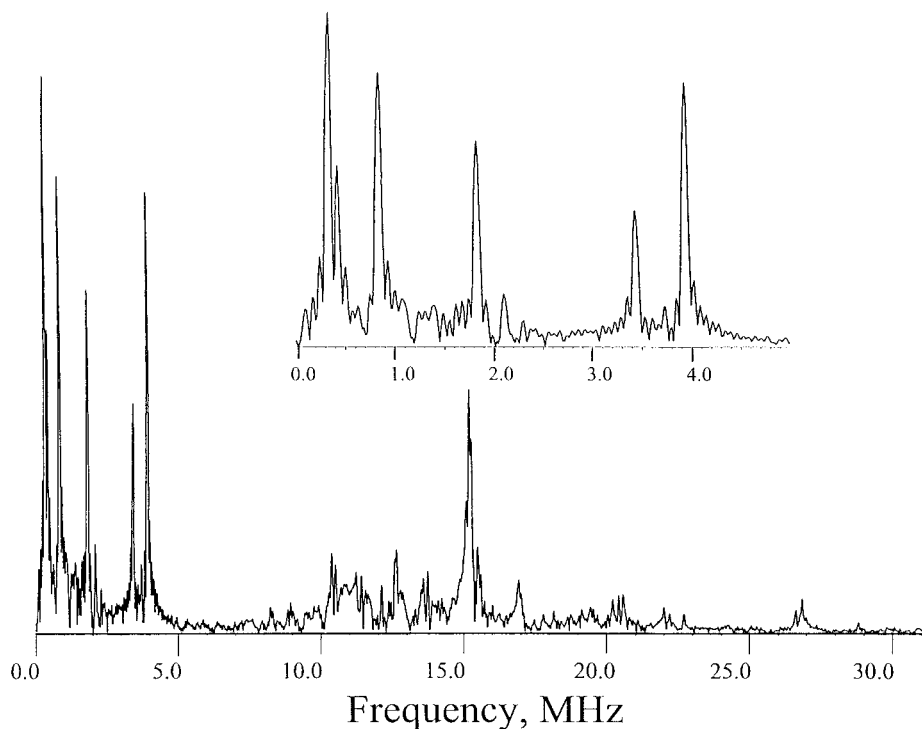


FIG. 6. Three-pulse ESEEM measurements of a Cu-His single crystal recorded at $B_0 = 3367$ G, at the same orientation as in Fig. 5. $\nu_{\text{MW}} = 9.7348$ GHz, $t_{\text{MW},\pi/2} = 16$ ns, $\tau = 288$ ns. The inset presents the expanded region between 0 and 4 MHz, containing the lines originating from the remote ^{14}N of the imidazole moiety.

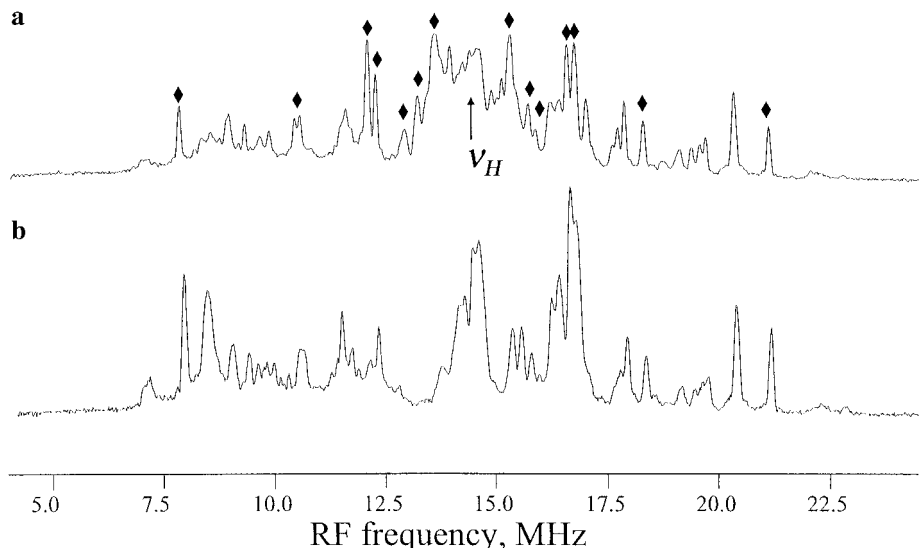


FIG. 7. ENDOR spectra of a Cu-His single crystal recorded at the same orientation and field as in Fig. 6. (a) Standard Davies ENDOR spectrum ($\tau = 288$ ns) recorded with long MW pulses (200, 100, 200 ns, respectively) and $\tau = 1 \mu\text{s}$. The diamonds mark the ^1H signals. (b) Same as (a) but short pulses (48, 24, 48 ns) and $\tau = 288$ ns. In both spectra $t_{\text{RF}} = 8 \mu\text{s}$ and $\Delta\text{RF} = 0.02$ MHz.

The Davies ENDOR spectrum, recorded with selective pulses and presented in Fig. 7a, is very congested in the 7- to 23-MHz region and comprises overlapping ^1H and ^{14}N signals. The ^1H doublets, which are symmetric about the ^1H Larmor frequency, ν_{H} , are indicated in the figure. Most of these doublets can be eliminated by recording the spectrum with shorter MW pulses that are nonselective with respect to small hyperfine couplings (Fig. 7b). The resulting spectrum therefore consists mainly of ^{14}N signals of the directly bound nitrogens. The ENDOR spectrum, presented in Fig. 9c, was recorded under the same conditions, with the exception that the stimulated echo pulse sequence was used for detection. It is identical to

the spectrum obtained with the standard Davies ENDOR sequence, except that the S/N is lower due to the generation of “unwanted” echoes (23).

The 2D ENDOR-ESEEM correlation spectrum, recorded at the same magnetic field as the ESEEM and ENDOR spectra shown in Figs. 6 and 7, is presented in Fig. 8. The vertical dimension, F2, represents the three-pulse FT-ESEEM spectrum (only the region of the ^{14}N is shown), while the horizontal dimension, F1, corresponds to the ENDOR spectrum. Following the connectivities of the cross peaks, the ESEEM peaks at 3.94, 1.83, 1.04, and 0.35 MHz are readily assigned to site I, whereas the 3.4- and 0.35-MHz lines are attributed to site II. The two sites overlap at 0.35 MHz. Using the correlations of the two intense ESEEM lines at 3.9 and 3.4 MHz, the ENDOR spectrum breaks into two subsets shown in the slices depicted in Figs. 9a and 9b, respectively. The two subsets are marked with full and empty triangles in the ENDOR spectrum shown in Fig. 9c. The ENDOR spectra of each site is relatively simple and several quartets, assigned to different ^{14}N nuclei are easily identified in each site. The additional nonmarked signals have not been assigned and may be attributed to ^{14}N or $^{35,37}\text{Cl}$.

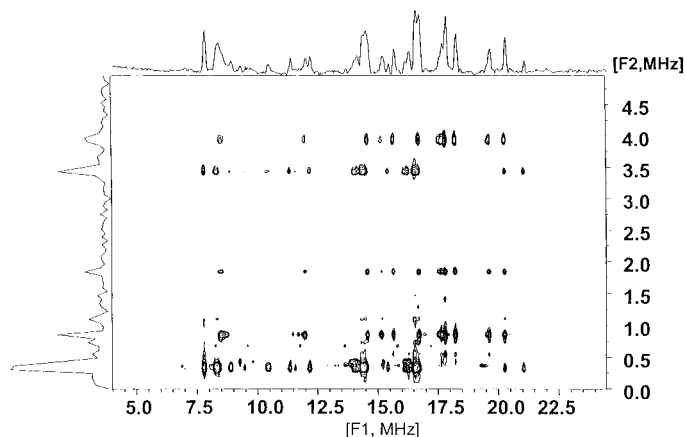


FIG. 8. A 2D ENDOR-ESEEM correlation spectrum of a Cu-His single crystal recorded at the same conditions and crystal orientation as in Figs. 6 and 7. $\nu_{\text{MW}} = 9.7438$ GHz, $\Delta\text{RF} = 0.04$ MHz, $\Delta T = 16$ ns, $t_{\text{RF}} = 8 \mu\text{s}$ (512×1024 , RF \times time).

SUMMARY

A new 2D experiment that provides correlation between ESEEM and ENDOR frequencies, designed to resolve nuclear frequencies of two different sites, was presented. The feasibility of the experiment has been demonstrated theoretically on a simple system, consisting of an $S = \frac{1}{2}$ electron coupled to two different nuclei with $I = \frac{1}{2}$, as well as experimentally on a Cu(II) doped L-histidine single crystal. The 2D spectra show

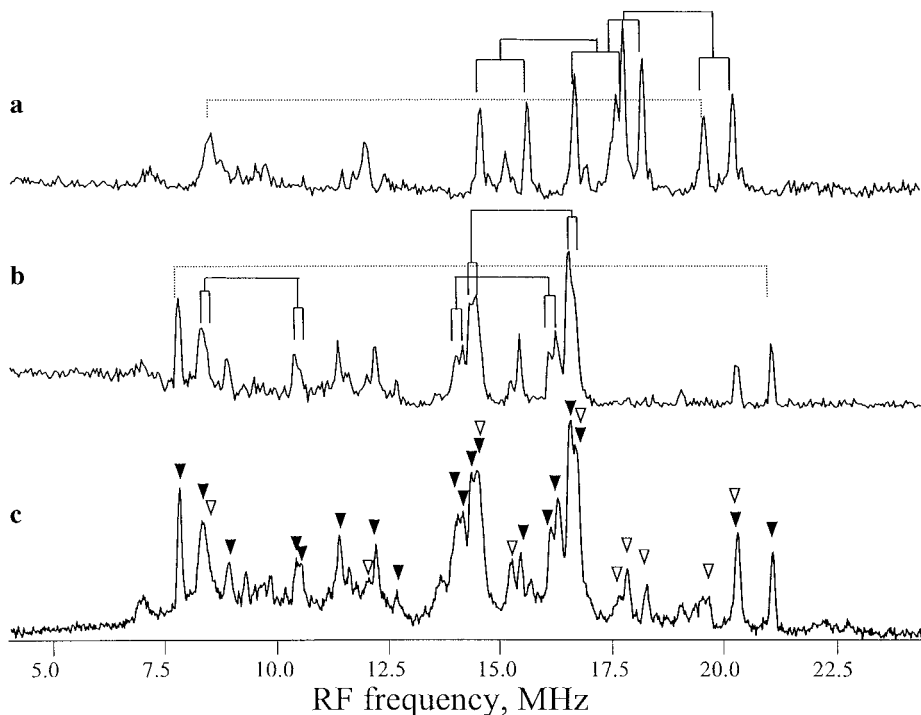


FIG. 9. Slices taken from the 2D spectrum shown in Fig. 8 along 3.94 MHz (a) and 3.4 MHz (b). Several ^{14}N quartets are indicated (solid lines) along with proton doublets (dotted lines) (c). For comparison the Davies ENDOR recorded with a stimulated echo detection ($\tau = 288$ ns, $T = 400$ ns, $t_{\text{RF}} = 8$ μs , and $\Delta\text{RF} = 0.02$ MHz), is shown as well. The empty and full triangles represent the two subsets as identified from the 2D experiment.

selective ENDOR-ESEEM correlations, which allowed the straightforward separation of the ESEEM and ENDOR spectra corresponding to different paramagnetic centers, thus facilitating significantly the assignment of the ^{14}N signals. To improve the resolution in the ESEEM dimension the two-pulse echo detection sequence in the Davies ENDOR experiment has been replaced with a stimulated echo sequence.

Although in this work the 2D ENDOR-ESEEM correlation experiment has been demonstrated on a single crystal, where both ESEEM and ENDOR lines are narrow and well resolved, it can be applicable to frozen solutions and polycrystalline samples as well, since ESEEM and ENDOR spectroscopies are routinely applied to orientationally disordered samples. Although such samples require more averaging, increasing the time of the experiment, the lower resolution allows for the acquisition of a smaller number of points in each dimension compared to single crystals, thus reducing the time of the experiment. For example, the 2D spectrum of the Cu-His single crystal was collected with 1024 points in the time domain in order to resolve the lines of the two sites. In orientationally disordered samples this can be reduced by a factor of 2 to 4 and the same argument holds for the RF domain. Therefore, the total time of the experiment is not expected to increase significantly. Besides the ability to resolve signals belonging to different species, the 2D ENDOR-ESEEM correlation experiment carried out in orientationally disordered samples, combined with orientation selection, can in principle,

provide information regarding the relative orientation of the hyperfine tensors involved. This information should be extracted from the specific lineshapes of the cross peaks.

ACKNOWLEDGMENTS

This research was supported by a grant from the Israel Science Foundation administered by the Israel Academy of Science and Humanities.

REFERENCES

1. G. Feher, Observation of Nuclear magnetic resonance via the electron spin resonance line, *Phys. Rev.* **103**, 834–835 (1956).
2. C. Gemperle and A. Schweiger, Pulsed electron-nuclear double resonance methodology, *Chem. Rev.* **91**, 1481–1506 (1991).
3. H. Kurreck, B. Kirste, and W. Lubitz, "Electron Nuclear Double Resonance Spectroscopy of Radicals in Solution," VCH, Weinheim, 1988.
4. W. B. Mims, Envelope modulation in spin-echo experiments, *Phys. Rev. B* **5**, 2409–2419 (1972).
5. W. B. Mims, Amplitudes of superhyperfine frequencies in electron-spin-echo envelope, *Phys. Rev. B* **6**, 3543–3545 (1972).
6. A. Schweiger, Pulsed electron spin resonance spectroscopy: Basic principles, Techniques and examples of applications, *Angew. Chem. Int. Ed. Engl.* **30**, 265–292 (1991).
7. L. Kevan, Modulation of electron spin-echo decay in solids, in "Time Domain Electron Spin Resonance," (L. Kevan and R. N. Schwartz, Eds.), Wiley, New York, 1979, pp. 279–341.
8. S. A. Dikanov and Yu. D. Tsvetkov, "Electron Spin Echo Envelope

- Modulation (ESEEM) Spectroscopy," CRC Press, Boca Raton, FL, 1992.
9. R. P. J. Merks and R. de Beer, Two-dimensional Fourier transform of electron spin-echo envelope modulation: An alternative for ENDOR, *J. Phys. Chem.* **83**, 3319–3322 (1979).
 10. P. Höfer, A. Grupp, H. Nebenführ, and M. Mehring, Hyperfine sublevel correlation (HYSCORE) spectroscopy: A 2D ESR investigation of the squaric acid radical, *Chem. Phys. Lett.* **132**, 279–282 (1986).
 11. A. Pöpl, J. Simon, and G. Völkel, ^1H one- and two-dimensional five pulse ESEEM investigations on a radiation center in betaine phosphite single crystals, *Appl. Magn. Reson.* **6**, 455–469 (1994).
 12. D. Goldfarb, V. Kofman, J. Libman, A. Shanzer, R. Rahmatouline, S. van Doorslaer, and A. Schweiger, Double Nuclear Coherence Transfer (DONUT)-HYSCORE—A New Tool for the Assignment of Nuclear Frequencies, *J. Am. Chem. Soc.* **120**, 7020–7029 (1998).
 13. M. Willer, J. Granwehr, J. Forrer, and A. Schweiger, Two-dimensional nuclear-Zeeman-resolved electron spin echo envelope modulation (NZ-ESEEM) spectroscopy, *J. Magn. Reson.* **133**, 46–52 (1998).
 14. G. Jeschke and A. Schweiger, Hyperfine-correlated electron-nuclear double resonance spectroscopy, *Chem. Phys. Lett.* **246**, 431–438 (1995).
 15. G. Jeschke and A. Schweiger, Time-domain chirp electron nuclear double resonance spectroscopy in one and two dimensions, *J. Chem. Phys.* **103**, 8329–8337 (1995).
 16. M. Hubrich, G. Jeschke, and A. Schweiger, The generalized hyperfine sublevel coherence transfer experiment in one and two dimensions, *J. Chem. Phys.* **104**, 2172–2184 (1996).
 17. S. van Doorslaer and A. Schweiger, A two-dimensional sum combination frequency pulse EPR experiment, *Chem. Phys. Lett.* **281**, 297–305 (1997).
 18. J. J. Shane, P. A. A. W. van der Heijden, E. J. Reijerse, and E. de Boer, An ESEEM investigation of single crystals and powders of copper-doped L-histidine hydrochloride monohydrate, *Appl. Magn. Reson.* **6**, 427–454 (1994).
 19. H. Thomann and M. Bernardo, Pulsed electron-nuclear multiple resonance spectroscopic methods for metalloproteins and metalloenzymes, *Methods Enzymol.* **227**, 118–189 (1993).
 20. E. R. Davies, A new pulsed ENDOR technique, *Phys. Lett. A* **47A**, 1–2 (1974).
 21. R. J. Cook and D. H. Whiffen, Relative signs of hyperfine coupling constants by a double ENDOR experiment, *Proc. Phys. Soc.* **84**, 845–848 (1964).
 22. M. Mehring, P. Höfer, and A. Grupp, Pulsed electron nuclear double and triple resonance schemes, *Ber. Bunsenges. Phys. Chem.* **91**, 1132–1127 (1987).
 23. J.-M. Fauth, A. Schweiger, L. Braunschweiler, J. Forrer, and R. R. Ernst, Elimination of unwanted echoes and reduction of dead time in three-pulse electron spin echo spectroscopy, *J. Magn. Reson.* **66**, 74–85 (1986).
 24. R. Hirasawa and H. Kon, Electron paramagnetic resonance and polarized absorption spectra of Cu(II)-doped single crystal of L-histidine hydrochloride monohydrate, *J. Chem. Phys.* **56**, 4467–4474 (1972).
 25. C. A. McDowell, A. Naito, D. L. Sastry, Y. U. Cui, K. Sha, and S. X. Yu, Ligand ENDOR Study of Cu(II)-doped L-histidine deuteriochloride monodeuterohydrate single crystals at 4.2 K, *J. Mol. Struct.* **195**, 361–381 (1989).
 26. M. J. Colaneri and J. Peisach, An electron spin-echo envelope modulation study of Cu(II)-doped single crystals of L-histidine hydrochloride monohydrate, *J. Am. Chem. Soc.* **114**, 5335–5341 (1992).
 27. U. Haeberlene, High resolution NMR in solids, selective averaging, in "Advances in Magnetic Resonance" (J. S. Waugh, Ed.), Suppl. 1, Academic Press, New York, 1976.
 28. C. Gemperle, G. Aebli, A. Schweiger, and R. R. Ernst, Phase cycling in pulse EPR, *J. Magn. Reson.* **88**, 241–256 (1990).